



# Aerodynamic Coefficients of Free-Flying Cubes in Hypersonic Flowfield

Patrick M. Seltner,\* Sebastian Willems,† and Ali Gülan‡  
*DLR, German Aerospace Center, 51147 Cologne, Germany*

DOI: 10.2514/1.A34345

Aerodynamic coefficients of a cube depending on a broad-range attitude change have been measured using the free-flight technique in a hypersonic flowfield. Experiments were performed therefore in the hypersonic wind tunnel H2K at the German Aerospace Center (DLR) in Cologne. The free-flight technique in H2K has allowed achieving a continuous rotation of the cube without any sting interferences in a broad angular range of 90°. This motion of the model during the free flight has been acquired using a nonintrusive high-speed stereo tracking system. A marker-based tracking algorithm has been applied to reconstruct the three-dimensional flight trajectories and attitudes to determine the resulting forces and moments. By using high-speed schlieren photography, the unsteady flow structures have been recorded. Pitch-angle-dependent aerodynamic coefficients of rotating cubes have been observed.

## Nomenclature

|                         |   |
|-------------------------|---|
| $a$                     | = acceleration, m/s <sup>2</sup>              |
| $C_D$                   | = aerodynamic drag force coefficient          |
| $C_F$                   | = aerodynamic force coefficient               |
| $C_L$                   | = aerodynamic lift force coefficient          |
| $C_M$                   | = aerodynamic pitching moment coefficient     |
| $f$                     | = frame rate, Hz                              |
| $g$                     | = acceleration of free fall, m/s <sup>2</sup> |
| $I$                     | = moment of inertia, kg m <sup>2</sup>        |
| $l_{ref}$               | = reference length, m                         |
| $Ma_\infty$             | = free-stream Mach number                     |
| $m$                     | = mass, kg                                    |
| $p_r$                   | = measured ram pressure, Pa                   |
| $p_{r,t}$               | = theoretical ram pressure, Pa                |
| $p_0$                   | = reservoir pressure, bar                     |
| $p_\infty$              | = free-stream static pressure, Pa             |
| $Re_\infty$             | = free-stream unit Reynolds number, 1/m       |
| $S_{ref}$               | = reference area, m <sup>2</sup>              |
| $T_0$                   | = reservoir temperature, K                    |
| $T_\infty$              | = free-stream static temperature, K           |
| $t$                     | = time, s                                     |
| $v_\infty$              | = free-stream velocity, m/s                   |
| $x, y, z$               | = Cartesian coordinates, mm                   |
| $\varphi, \theta, \psi$ | = Euler angles, °                             |
| $\kappa$                | = ratio of specific heat                      |

## Subscripts

|     |                     |
|-----|---------------------|
| $i$ | = dimension index   |
| $j$ | = index             |
| 0   | = initial condition |

## I. Introduction

THE ability to reliably predict the atmospheric reentry trajectories of deorbiting space debris, meteoroid fragments, or components of launch-vehicle stages is of great importance to avoid damage to persons or properties on ground. Therefore, it is necessary to predict the impact region as well as size and mass of remaining fragments with a reasonable reliability. For this purpose, the forces and moments of uncontrollably flying objects have to be known. Much of previous work exploring the forces on single simple-shaped bodies in super- and hypersonic flows has been conducted to determine the influence factors (e.g., Reynolds number, Mach number, ballistic coefficient, and roughness) on aerodynamic drag. Spherical bodies, on the one hand, are adequately studied test objects as in [1–6], which is relevant for the trajectory modeling of meteoroid entries. These studies point out an independence of the drag coefficient on the Mach number under hypersonic conditions with an approximate value of  $C_D = 0.92$  [3]. On the other hand, less studies were carried out on other blunt bodies like cubes [3,7,8], which are of some interest in the context of space debris behavior (e.g., CubeSats) during entry into the Earth atmosphere. Hansche and Rinehart [7] have shown the dependence of the Mach number on the aerodynamic drag coefficient for rotating cubes free-flying in sub-, trans-, and supersonic flows. A rough convergent value of  $C_D = 1.66$  for higher Mach numbers ( $Ma_\infty > 4.0$ ) is given by Hoerner [3].

These prior studies deal purely with the drag, whereas the other forces and moments like lift or pitching moment are neglected. Furthermore, the aerodynamic coefficients in [7] are not related to determined orientation angles of the cubes, because the test objects rotate uncontrollably and its attitudes are not measured over the entire time. In addition, this work provides only little information about the aerodynamic behaviors of cubes in hypersonic flows. Because of the measuring technique of distance-time tracing by Hansche and Rinehart [7], using a chronograph with six grid stations, the quality of measuring data is poor. Also the measurement with strain gauge balances as in [6] is affected by interactions of the wake flow with the sting.

Hence, the purpose of the present study is to determine the effect of the body orientation on the aerodynamic drag, lift, and pitching moment of cubes in a hypersonic flow facilitating more accurate orbital-debris atmospheric-reentry prediction of tumbling cubic bodies. The focus of this paper is on the influence of the pitch angle. In addition, the static stability behavior of the object has been studied. To ensure this, a state-of-the-art free-flight technique in combination with a stereo tracking system is employed to obtain more accurate results without flow interferences with the measuring device like stings or support arms and higher temporal resolutions.

In the second section of this paper, the experimental tools and setup are described. The postprocessing description with six-degree-of-freedom (6DoF) motion tracking and the method for the determination

Received 5 July 2018; revision received 26 April 2019; accepted for publication 24 August 2019; published online 20 September 2019. Copyright © 2019 by DLR e.V. (German Aerospace Center). Published by the American Institute of Aeronautics and Astronautics, Inc., with permission. All requests for copying and permission to reprint should be submitted to CCC at www.copyright.com; employ the eISSN 1533-6794 to initiate your request. See also AIAA Rights and Permissions www.aiaa.org/randp.

\*Research Scientist, Supersonic and Hypersonic Technologies Department, Linder Höhe; patrick.seltner@dlr.de.

†Research Scientist, Supersonic and Hypersonic Technologies Department, Linder Höhe; sebastian.willems@dlr.de.

‡Department Head, Supersonic and Hypersonic Technologies Department, Linder Höhe; ali.guelhan@dlr.de. Member AIAA.

of aerodynamic coefficients will follow this part. Finally, the discussion of the results will complete the paper.

## II. Experimental Setup

Wind tunnel experiments were conducted with rotating cubes at a Mach number of 7.0, whereby the positions and attitudes are tracked during the entire free flight. This was possible by the use of a high-speed optical stereo tracking system measuring model motion in 3D space. By performing a 6DoF motion tracking, the flight trajectories and attitudes were reconstructed from which the aerodynamic drag, lift, and pitching moment were determined. Furthermore, schlieren images were recorded to characterize flow structures around the bodies.

### A. Hypersonic Wind Tunnel Cologne (H2K)

#### 1. General

All experiments were carried out in the Hypersonic Wind Tunnel Cologne (H2K) at the Supersonic and Hypersonic Technologies Department of the German Aerospace Center (DLR). This facility is a blowdown wind tunnel with a free-jet test section and a nozzle exit diameter of 600 mm. There are replaceable rotationally symmetric contoured nozzles for the design Mach numbers of 5.3, 6.0, 7.0, 8.7, and 11.2, facilitating an axially symmetrical homogenous flow. Eight electrical resistance heaters with a total maximum electrical power of 5 MW enable stagnation temperatures up to 1000 K. Moreover, a maximum stagnation pressure of 55 bar is possible, whereas the rate of mass flow is limited to 20 kg/s. The typical test conditions for the conducted experiments are given in Table 1, whereby the viscosity of air needed for the Reynolds number calculation is determined by the use of Sutherland's formula as in [9] with a linear interpolation for the low-temperature regime.

The H2K is a pressure-vacuum wind tunnel, whereby dry air from 60-bar reservoirs is heated in the electrical heaters to prevent condensation of the fluid during the expansion or to study aerothermal heating effects. After the desired temperature is reached, the pressurized air is released through a settling chamber and expands afterward in one of the differently contoured Laval nozzles to develop a free jet. The measurement chamber is connected with a diffuser and a heat exchanger. Because of the required high pressure ratio to develop a stable hypersonic free jet for approximate 30 s, a vacuum sphere completes the facility to prevent a rapid growth of the chamber pressure in the test section. Further details on the test facility can be found in [10].

#### 2. Flow Characterization of the Mach-7 Nozzle

The Mach-7 nozzle was in use for the present aerodynamic testing. The flow at the nozzle exit plane has a fully developed turbulent boundary layer, which is turned in a shear layer for the free jet. In Fig. 1 the ratio of locally measured ram pressure to theoretical ram pressure for the Mach-7 nozzle with an unit Reynolds number of  $Re_{\infty} = 8.3 \cdot 10^6 / m$  from calibration tests is presented as slices of the horizontal, vertical, and axial plane. The theoretical ram pressure is calculated with Eq. (1) using the stagnation pressure ratio over a normal shock.

$$p_{r,t} = p_0 \left[ 1 + \frac{2\kappa}{\kappa+1} (Ma_{\infty}^2 - 1) \right]^{-(1/\kappa-1)} \left[ 1 - \frac{2}{\kappa+1} \left( 1 - \frac{1}{Ma_{\infty}^2} \right) \right]^{-(\kappa/\kappa-1)} \quad (1)$$

For this nozzle calibration, a measuring rake was in use, which was equipped with 29 pitot probes in a plane, as described in [10]. This

**Table 1** Typical test conditions

| $Ma_{\infty}$ | $p_0$ , bar      | $T_0$ , K | $p_{\infty}$ , Pa | $T_{\infty}$ , K | $v_{\infty}$ , m/s | $Re_{\infty}$ , $10^6 / m$ |
|---------------|------------------|-----------|-------------------|------------------|--------------------|----------------------------|
| 7.0           | 5.2              | 600       | 126               | 56               | 1046               | 2.1                        |
| 7.0           | 4.8 <sup>a</sup> | 600       | 116               | 56               | 1046               | 2.0                        |

<sup>a</sup>Second test series with different flow condition.

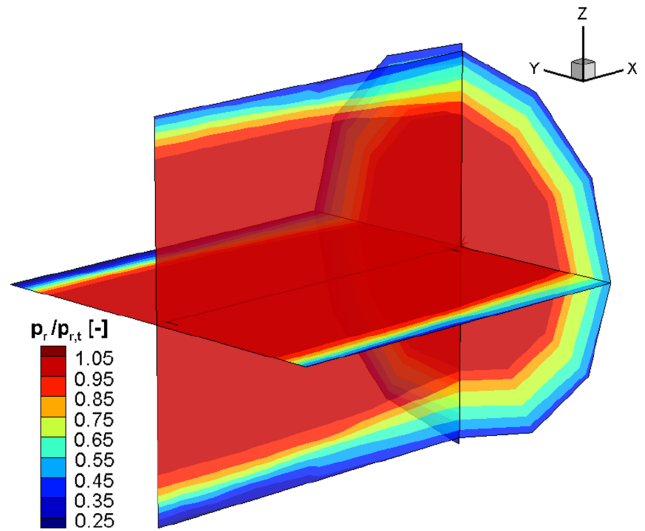


**Fig. 1** Ratio of locally measured ram pressure to theoretical ram pressure of the free jet for the Mach-7 nozzle (flow conditions:  $p_0 = 23.5$  bar,  $T_0 = 662$  K,  $Re_{\infty} = 8.3 \cdot 10^6 / m$ ); flow direction is the positive  $x$  direction; core flow is defined by the red area.

rake was rotated each  $30^\circ$  from  $0^\circ$  to  $180^\circ$  and displaced each 20 mm along the flow direction from nozzle exit with  $x = 0$  to 580 mm. Thus, each axial plane is resolved by 203 measuring points.

The usable homogeneous core flow is defined by a local ram pressure deviation of 5% in relation to the theoretical ram pressure (Fig. 1). The cross section of the core flow is declining with increasing distance from the nozzle exit because of the growing shear layer.

This cross-sectional area is dependent on the Reynolds number as well. A decreasing Reynolds number results in a thicker boundary layer at the nozzle exit as well as a thicker shear layer of the free jet, whereby the Mach-number-defining proportion of nozzle exit to narrowest cross section decreases as the Mach number decreases [10]. Thus, the design Mach number of the nozzle has to be corrected by the Reynolds number. This was considered for the free-stream Mach number in Table 1. Furthermore, it should be noted that this calibration data ( $Re_{\infty} = 8.3 \cdot 10^6 / m$ ) do not perfectly represent the ram pressure field of the present measurements ( $Re_{\infty} = 2.1 \cdot 10^6 / m$ ) due to different shear layer thicknesses.

## B. Model Setup

The model in this study is a single steel cube as shown in Fig. 2. It has an edge length of  $50.30 \pm 0.06$  mm and a mass of  $981.33 \pm 0.03$  g. For the application of the marker-based stereo tracking technique, the surface of the cube is varnished matt-white with matt-black circular point markers.

The magnetic cube is held by an electromagnet and released by cutoff of the power. Compared with the mounting of spheres with dental flosses as in [11], this release mechanism does not leave residues on the model surface.

In this experimental setup (shown in Figs. 3 and 4), the holding electromagnet with the cube is fixed above the free jet. This holding position defines the initial pitch angle  $\theta_0$ . Before the run, the measurement chamber is under vacuum condition. After initiating the flow, the free jet needs 2–3 s to stabilize. The electromagnet is switched off and the cube begins to fall. First, the test article is free-falling in vacuum. When the cube enters the shear layer of the jet, it begins to rotate because of the increasing stagnation pressure (shown in Fig. 1), resulting in an inhomogeneous surface pressure distribution. Then, the model passes the homogenous core flow before it crosses the lower part of the shear layer. Finally, it is caught at the bottom of the test section. This free fall takes approximately 0.4 s, whereby the free-flight time in the core flow for analysis purposes is about 0.1 s.

For the present research, the vertical and streamwise forces lift ( $C_L$ ) and drag ( $C_D$ ) as well as the pitching moment ( $C_M$ ) are in the



Fig. 2 Cubic model covered with spherical point markers.

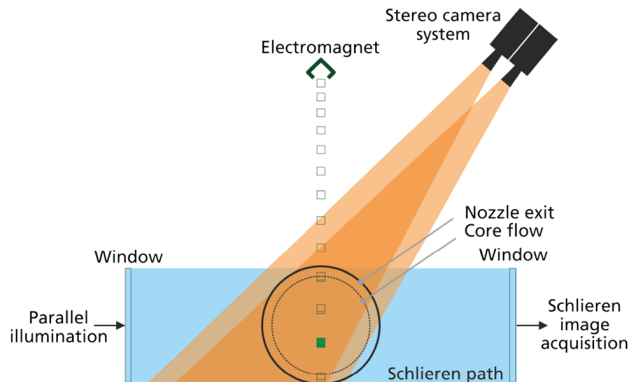


Fig. 3 Schematic layout of the experimental setup.

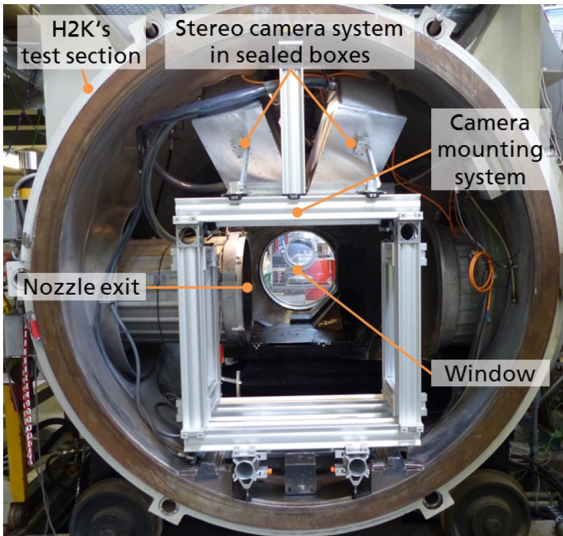


Fig. 4 Experimental setup in H2K's test section.

focus. Figure 5 depicts the reference frame of these aerodynamic coefficient components with respect to the global coordinate system (GCS) (red axes), which is spatially fixed on the nozzle exit plane. The  $x$  direction of this GCS is defined by the nozzle axis pointing downstream as the  $z$  direction is aligned with the reversed gravitational vector, whereas the  $y$  and  $z$  axes are in the nozzle exit plane. In contrast to that, the local coordinate system (LCS) of the cube is body fixed, which is needed to determine the orientation angles, whereas the aerodynamic coefficients (blue axes) are defined in the global coordinate system. In Fig. 5, an edge-exposed configuration is

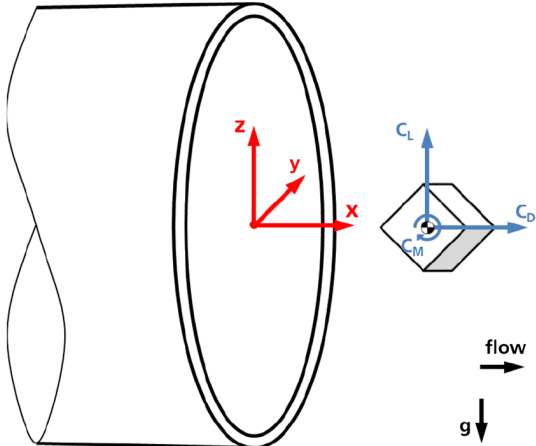


Fig. 5 Global coordinate system with respect to nozzle exit and geometrical definition of the aerodynamic coefficients.

shown, whereby the line from one cube's edge center to its center of gravity (CoG) is parallel to the global  $x$  axis. Further orientation designations are used in this paper like plane-exposed and corner-exposed. The former is defined by a parallelism of global  $x$  axis and surface normal of the cube, whereas the line from one corner to the CoG of the test object is parallel to the  $x$  axis of the GCS for the latter.

### C. Instrumentation

#### 1. High-Speed Schlieren Photography

A Z-type schlieren photography setup with a knife-edge was used, as described in [12]. The diameter of the concave mirrors is 500 mm and the focal length is 4000 mm. The applied focusing lens has a focal length of 150 mm. As a light source, a 1000 W xenon arc lamp was used. For the acquisition of image sequences, a Photron FASTCAM APX-RS model 250K high-speed camera with a monochrome CMOS sensor was used that provides frame rates up to 3 kHz at full  $1024 \times 1024$  pixels resolution. This maximum frame rate at full frame was used in this study that allows the high-speed recording of the model motion and flow structures as the bow shock and the wake region. The exposure time was  $2 \mu\text{s}$ .

#### 2. High-Speed Stereo Image Acquisition

A further optical system was integrated in the measurement chamber for marker-based model tracking consisting of two synchronously recording Photron FASTCAM SA-X2 model 480 K monochrome high-speed cameras in stereoscopic arrangement. Each camera was equipped with a Titanar B24 measuring lens having a focal length of 24 mm. The integration of the cameras in the test section has two major causes: minimizing optical effects because of density changes due to ambient air and enabling an optimal perspective. This setup ensures the observation of a measuring volume of  $525 \text{ mm} \times 565 \text{ mm} \times 565 \text{ mm}$ . These two cameras were covered in sealed boxes to prevent an overheating due to the ambient vacuum. Moreover, a stiff mounting of the stereo camera system was guaranteed so that it is resistant to vibration leading to decalibration.

For both cameras, a frame rate of 12 kHz was set. This high frame rate at full  $1024 \times 1024$  pixels resolution was used because of the short free-flight time in a split second and to acquire sufficient data points for high-quality results after postprocessing. Because of a short exposure and a small aperture, a light source with high intensity is essential to acquire high-contrast images. Therefore, four 86 W plus four 38 W high-power LEDs with a color temperature of 5000 K were mounted onto an aluminum ring, which functions as capacitive cooler. Another reason for the use of this light source is the cold-white property ensuring a high yield of FASTCAM series blue-sensitive CMOS sensors. Each camera was equipped with one of these LED aluminum rings that are concentrically mounted on the camera boxes. This benefits an optimal illumination.

As an example for displacement determination by stereo tracking, Fig. 6 depicts the three-dimensional components of the position of a

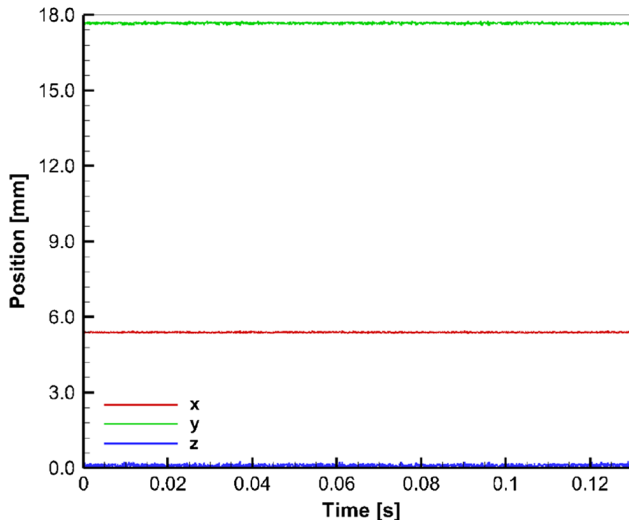


Fig. 6 Position of a fixed reference point in a reference measurement.

fixed reference point being acquired with the same experimental setup as in the wind tunnel tests. These data are used to determine the position accuracy of the stereo tracking technique for the present measurements. The standard deviations in  $x$ ,  $y$ , and  $z$  are 16, 31, and 48  $\mu\text{m}$ , respectively.

### 3. Facility Data Acquisition

During the wind tunnel run, the operating conditions were recorded with a sampling rate of 20 Hz. Here, the reservoir pressure was measured by GE Drucks absolute pressure transducer PDCR 921 and acquired by National Instruments 24-bit high-speed bridge module PXIe-4331. For the acquisition of reservoir temperature, a thermocouple type K class 1 from MTB Sensor-Technik, in combination with National Instruments 24-bit data acquisition card PXIe-4353, was employed. The total accuracies of the sensors were  $\pm 7 \text{ kPa}$  based on the full-scale value for the reservoir pressure and  $\pm 1.5 \text{ K}$  of the actual value for the reservoir temperature.

## III. Postprocessing

In this section, the data reduction is described, beginning the process with the recorded image pairs to determine the three-dimensional model trajectory as well as its flight attitude by the use of the digital image correlation (DIC) method with the subsequent postprocessing of the 6DoF motion tracking. These two parts are performed by the commercial stereo tracking software ARAMIS Professional 2017. With the 6DoF motion data consisting of CoG positions and orientation angles, it is possible to calculate the forces and moments over time by filtering and differentiation to receive afterward their aerodynamic coefficients. The schematic postprocessing description is shown in Fig. 7 and explained in the following subsections.

### A. Digital Image Correlation

In general, DIC is a photograph-based method using cross-correlations for noncontact deformation and motion analysis providing data about displacement and strain [13]. DIC-based stereo tracking was applied for the present investigation to process sequences of synchronous image pairs. Thus, the time-resolved measurement of three-dimensional motion vector is possible that enables the calculation of velocities and accelerations as well. Its functional principle is described below and explained with more details in [14,15].

First, the point markers on the gray-value measuring images have to be detected by ellipse fitting enabling a subpixel resolution for the applied method. The centers of these ellipses are the measurement points. Second, the three-dimensional world point coordinates of point markers are reconstructed by means of triangulation. Therefore,

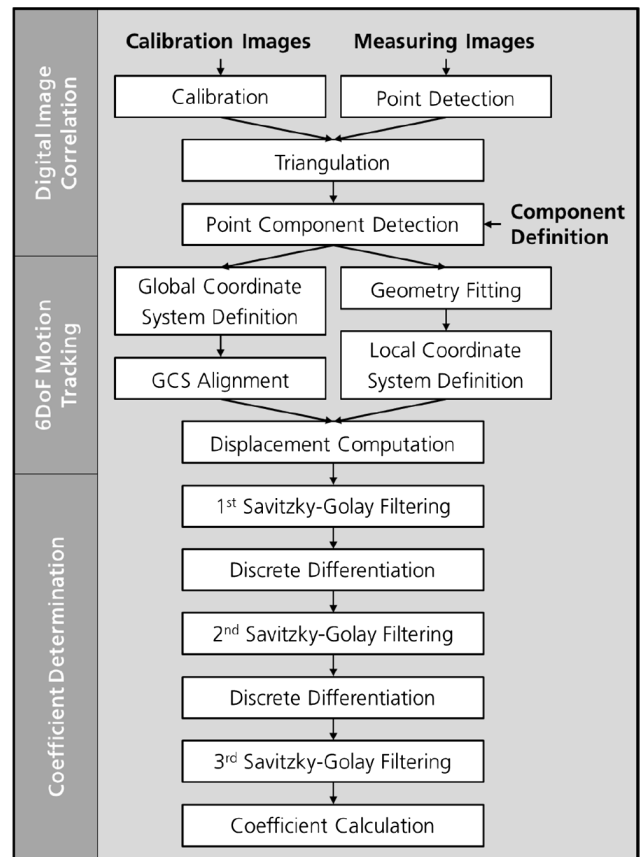


Fig. 7 Postprocessing description of the force and moment measurement.

calibration parameters are required. An image series of a differently positioned calibration object with known coordinates of reference point markers is recorded, which is processed to provide information about the extrinsic (e.g., position and orientation of each camera relating to the 3D space) and intrinsic camera parameters (e.g., focal length of camera lens as well as pixel size and resolution of the image sensor). The last-mentioned parameters are used to determine a correction function of optical distortions. Third, point components are defined by grouping points of the same object and afterward detected at different stages employing point-to-point distances of measuring point triangles.

### B. Six-DoF Motion Tracking

The DIC-tracked point markers can be used to determine the three positions in streamwise ( $x$ ), spanwise ( $y$ ), and vertical ( $z$ ) direction as well as the orientations roll ( $\varphi$ ), pitch ( $\theta$ ), and yaw angle ( $\psi$ ) of the test object with respect to the GCS.

First of all, the static reference component with at least three points is used to define a fixed GCS. The coordinate axes of this GCS have to be aligned for accurate measurement data such that the  $x$  axis is aligned streamwise and the  $z$  axis is parallel to the force of gravity. On that account, an additional free-fall (without flow) plus a free-flight (with flow) test with a single sphere were performed and post-processed. For the correct  $z$ -axis alignment, the trajectory of free-falling sphere is used to determine the direction of gravity. The computed free-flying trajectory and the  $z$  axis define a plane, whose normal is the  $y$  axis of the GCS.

Subsequently, a cubic CAD geometry with an edge length of 50.3 mm is fitted on the tracked surface points of the body. An LCS is defined in such a way that its origin is tacked on the CoG of the geometry and its coordinate axes are normal to the base areas of the cube for this particular shape.

Taken both coordinate systems together, the three-dimensional angular and translational displacements of the free-flying object with regard to the mentioned GCS are computed.

### C. Coefficient Determination

These motion data are slightly noisy because of the optical and processing deviations of the stereo tracking method as well as residuals of the geometry fitting. The signal-to-noise ratio is unfavorable due to the short time steps. Especially, the acceleration computation is very sensitive for noise in the position and orientation angle data due to the double derivation leading to quadratic noise growth. Hence, several signal-processing steps (Fig. 7) are necessary to compute useful aerodynamic coefficients. First, the signals are smoothed by filtering and derived by discrete differentiation twice to obtain the translational and angular velocities as well as the accelerations. Then, the second-derivative signals are smoothed again.

A conventional Savitzky–Golay filter is used for the present study, which fits piece-by-piece polynomial functions to the noisy signal by the least squares method [16,17]. In particular, the Savitzky–Golay filter ensures a digital smoothing without completely cutting off high-frequency proportions. Thus, the distribution of local extrema and variation remains unchanged. During the postprocessing of the present work, this filter was always set as linear polynomial with successive subsets of 161 adjacent data points for each value.

The discrete differentiation of the motion data with respect to time is performed by central finite-difference approximation as in [18]. In comparison to forward or backward methods, central difference features a second-order accuracy and prevents also time shifts of the derived signals.

At the end, the force and moment coefficients are calculated by using Eqs. (2) and (3), whereby the reference area in this study is defined as the square base area of the cube ( $S_{\text{ref}} = l^2$ ). In these formulas, the translational ( $a_i$ ) and angular accelerations ( $\ddot{\theta}$  for pitching) are determined by means of the double time derivation based on the position and orientation data. Because of the experimental setup, the vertical force coefficient is superposed by the gravity. This amount is subtracted for the determination of the lift coefficients. The aerodynamic coefficients are evaluated only in phase of steady-state free-stream conditions as well as when the test object is completely inside the homogenous core flow to minimize the effect of the stagnation pressure deviation on the resulting accelerations. A free-fall acceleration of  $g = 9.81127 \text{ m/s}^2$  is used for the calculation as given in [19].

$$C_{F_i} = \frac{ma_i}{(\kappa/2)Ma_{\infty}^2 p_{\infty} S_{\text{ref}}} \quad (2)$$

$$C_M = \frac{I_y \ddot{\theta}}{(\kappa/2)Ma_{\infty}^2 p_{\infty} S_{\text{ref}} l_{\text{ref}}} \quad (3)$$

## IV. Results

The main objective of the following analysis is to understand the complex dynamic behaviors of tumbling cubes in hypersonic flows by focusing on the effect of the variation of a single orientation angle on the motion characteristics provoked by aerodynamic forces and moments. For this purpose, the vertical and streamwise forces lift ( $C_L$ ) and drag ( $C_D$ ) as well as the pitching moment ( $C_M$ ) are of principal interest. Hence, the following two subsections (Secs. IV.A and IV.B) give direct experimental results from the schlieren photography and the stereo tracking system, respectively, whereas the results of Sec. IV.C concentrate on its motion derivatives after postprocessing as well as the static stability of cubes.

### A. Flow Structures and Model Motions

The parameter being varied in this present experimental study was the initial pitch angle  $\theta_0$ , whereby  $\theta_0 = 0^\circ$  means that a plane of the cube is orthogonal to the inflow. This configuration is called plane-exposed as described in Sec. II.B. For all experimental results being presented hereinafter, the initial roll and yaw angle were approximately zero, excepting a single run of an initially corner-exposed cube adding an initial yaw. Figure 8 shows sequences of schlieren images from these measurements. These configurations were chosen

to cover a broad range of pitch angles during free-flight as well as to avoid complications of additionally induced roll or yaw rotations. The duration between the first and last image of each series is 60 ms while the test article is passing the core flow.

The runs of Fig. 8 show a counterclockwise body rotation initiated by traversing the shear layer. While entering the upper shear layer, the test object experiences a negative pitching moment because of increasing stagnation pressure resulting in an asymmetric surface pressure distribution with a higher ram pressure on the lower body part (compare with  $p_r/p_{r,t}$  in Fig. 1). This is quite different for  $\theta_0 = -30^\circ$  and  $\theta_0 = -20^\circ$  (shown in Figs. 8a and 8b) as the pitch seems to be constant because of an additional oppositely turning moment provoked by the angular position with respect to the flow direction. Thus, the rotation of cubes in the present measurements is determined by two effects: shear-layer-initiated and body-orientation-initiated aerodynamic moments. Moreover, no obvious rolling or yawing motions appear for the pitch-only configurations (with  $\varphi_0 = 0^\circ$  and  $\psi_0 = 0^\circ$ ).

The flow structures in Fig. 8 exhibit always detached bow shocks whose shape depends on the flow angle relatively to the cube. This happens, because the required flow deflection angle, to follow the contour, of one or both front planes is larger than the maximum possible value for  $Ma_{\infty} = 7.0$ . For more plane-exposed models, it appears as a curved shock with a great shock stand-off distance like in Fig. 8d. By turning the leading edge more into the flow, this stand-off distance decreases and the shock becomes oblique at some point (visualized in Figs. 8b and 8e). Furthermore, low-density regions occur at the body edges due to expansion coming from the deflection and consequently an acceleration of the flow. These expansion fans interact with the bow shock, resulting in a curvature of the shock wave. Closely downstream of the leading edge, a second weak oblique shock becomes visible in some configurations (e.g., Figs. 8c and 8d). This attached shock is merging downstream with the bow shock.

A more complex flowfield and model motion of a three-dimensional rotation is presented in Fig. 9. Here, the bow shock appears weaker with a marginal shock stand-off distance, is less curved, and exhibits more oblique parts in comparison to the only-pitch configurations. No or only tenuous expansion fans at cube's corners can be seen in the schlieren images. These three-dimensional aerodynamic effects are barely visible in the two-dimensional view, because the depth of the phenomenon is too low for this integral-working optical system as well as the object is hiding some of these features.

For a plane-exposed cube, the flowfield with a schematic description of aerodynamic phenomena is shown in Fig. 10. Here, the hypersonic flow is compressed in front of the cube developing a bow shock. In the region of the stagnation streamline, this shock is normal. The stagnation streamline experiences the maximal deceleration. Moreover, the bow shock becomes more oblique downstream with lessening strength ending in an infinitely weak Mach wave. In comparison to the bow shock shape of a sphere in [20], the cube's one is more plane and its shock angle decreases less downstream to strongly slow down the flow over a wide frontal area. Between the bow shock and the face area, a thin broad subsonic region enables a strong outward deflection of the flow. The sonic line in Fig. 10 encloses this area. Afterward, the flow is deflected in opposite direction as well as accelerated by an expansion fan originating from the edge. At this point the flow is not able to follow the contour, resulting in very small separation bubble similar to the separation with reattachment downstream of a backward-facing step in [21]. A weak reattachment shock, which is visible in Fig. 10, deflects the flow in this way that the streamlines close to the wall are parallel to the contour. Further downstream, a second expansion fan at the trailing edge leads to an inward flow direction, causing an acceleration and separation of the flow. The resulting wake region with counter-rotating vortices narrows with larger distance to the rear. At its shear layer, compression waves appear due to its concave shape, resulting in an oblique shock at their intersection.

For an edge-exposed cube, Fig. 11 shows nearly the same aerodynamic phenomena as for the plane-exposed configuration with

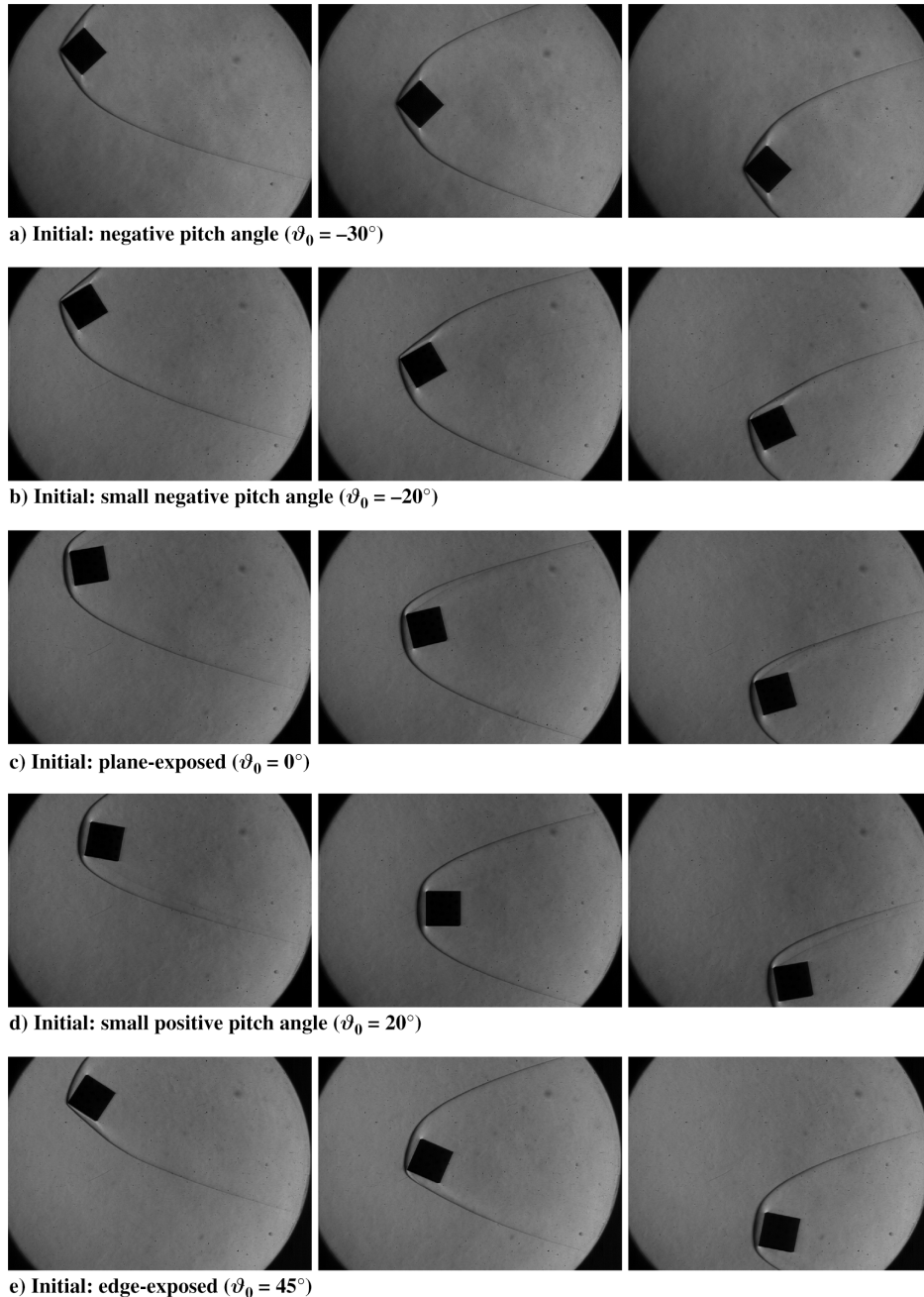


Fig. 8 Schlieren image sequences of pitch-only configurations showing the motion behavior in free-flight.

exception of some characteristics on the forebody. On the leading edge, the bow shock is detached with a small nonzero shock stand-off distance and a narrow subsonic region, because the  $45^\circ$  inclination angle of upper and bottom side is higher than the maximal flow deflection angle for the present Mach number. Further downstream of the stagnation point, the shock wave appears oblique until it interacts with the expansion fans from the top and bottom edge, resulting in a bending of the shock over the length of interaction. The reflecting

expansion waves are not visible on the schlieren image due to weakening. Moreover, no separation bubbles with subsequent reattachment shocks arise. In comparison to the plane-exposed cube, this orientation exhibits higher bow shock radii further downstream.

#### B. Flight Trajectories

The reconstruction of the rigid body motion by stereo tracking allows the determination of the three-dimensional single components

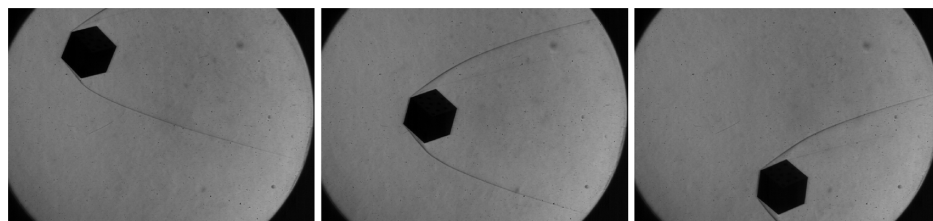


Fig. 9 A schlieren image sequence of an initially corner-exposed cube in free flight.

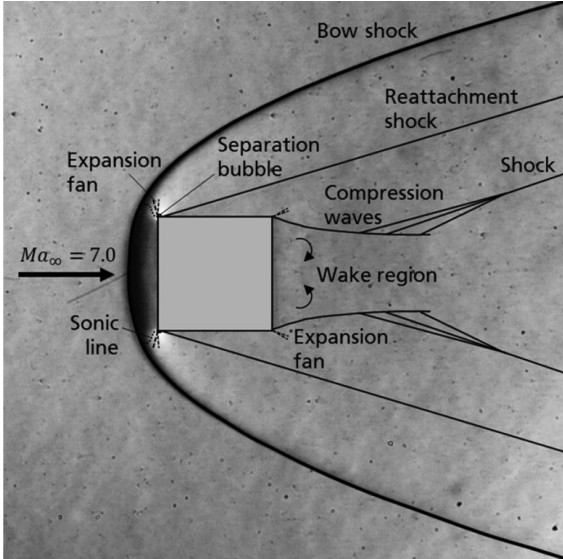


Fig. 10 Qualitative flowfield of one cube's plane is exposed to the flow.

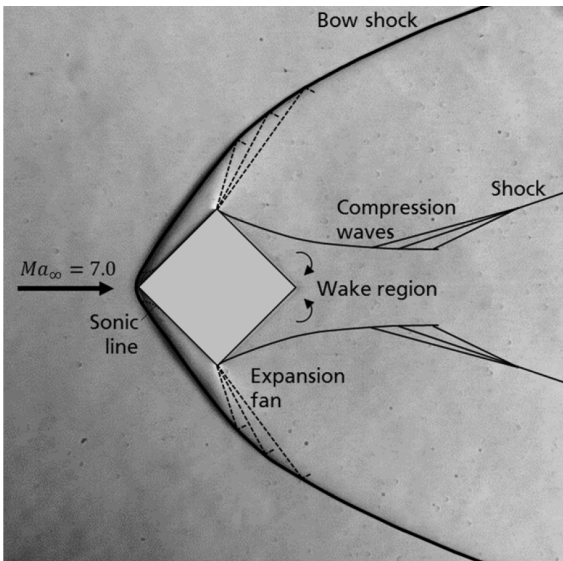


Fig. 11 Qualitative flowfield of one cube's edge is exposed to the flow.

of position and orientation angle. As an example, Fig. 12 shows the angular (roll, pitch, and yaw) and translational (streamwise, spanwise, and vertical) displacements of a rotating cube configuration

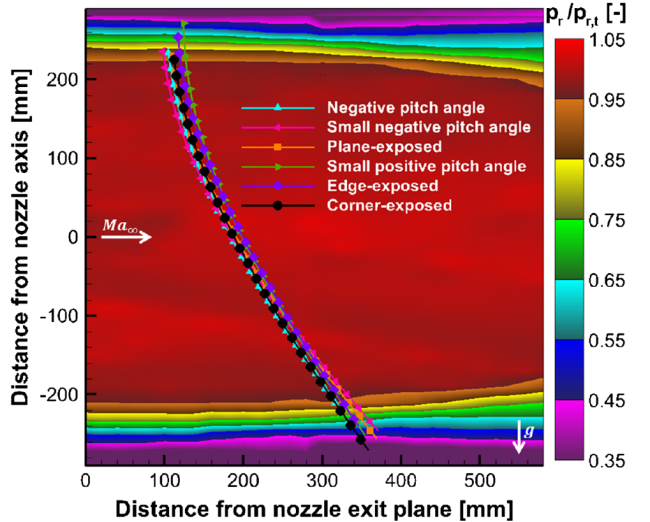


Fig. 13 Flight trajectories and flowfield characteristics of H2K's Mach-7 nozzle.

with an initial pitch angle of  $20^\circ$ . Because of the mirror-symmetrical shape of this model, the motion behavior is as expected two-dimensional. As there is neither initial roll nor initial yaw angle, the body experiences merely a streamwise ( $\Delta x = 167$  mm) and a vertical ( $\Delta z = -369$  mm) movement as well as a pitch rotation ( $\Delta\theta = 35^\circ$ ). However, the spanwise ( $\Delta y = -2$  mm), roll ( $\Delta\varphi = 2^\circ$ ), and yaw ( $\Delta\psi = -2^\circ$ ) motion components are almost constant and close to zero. Here, the covered pitch angle is 23 times and 17 times higher, respectively, than the total roll and yaw displacement (see Fig. 12). Therefore, the spanwise, roll, and yaw components are neglected and the problem is reduced to a 3DoF analysis.

All two-dimensional CoG trajectories in  $x$  and  $z$  directions relatively to the center of the nozzle exit plane are plotted in Fig. 13, showing the ram pressure distribution of the free jet at  $Ma_\infty = 7.0$  as a color contour layer as well. As expected, the cube experiences a streamwise acceleration. The most visible feature of Fig. 13 is that the flight trajectories are close together, whereby the streamwise displacement in the core flow ranges between 167 mm (green line) and 203 mm (pink line). However, these peak values do not permit a proper qualitative comparison with respect to the drag because the residence time in the jet core of all runs is different, varying between 113 ms (green line) and 126 ms (pink line). Thus, it is necessary to analyze the single components of the motion derivatives.

### C. Aerodynamic Forces and Moments

In this section, the resulting motion derivatives are described. Figure 14 shows the force coefficients in streamwise (drag) and

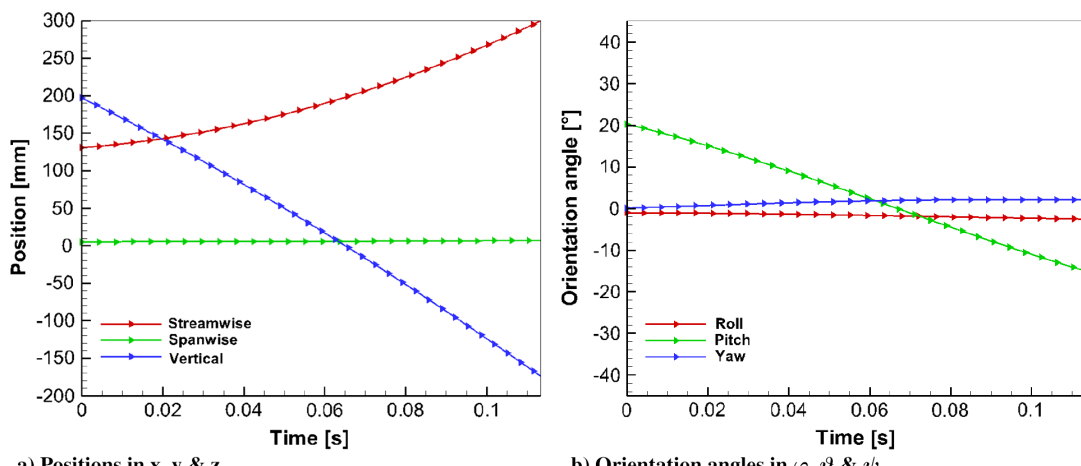
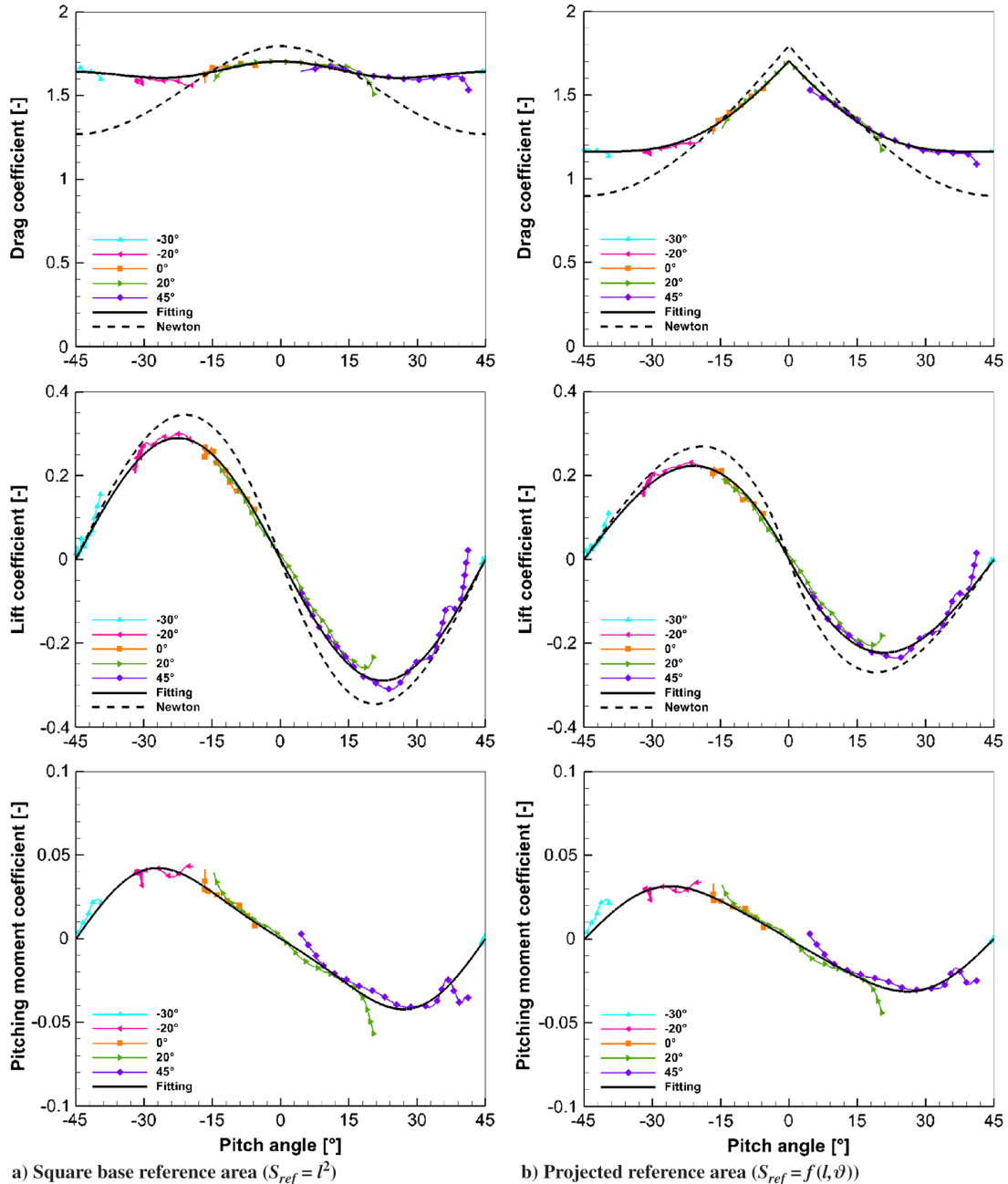


Fig. 12 Six-DoF motion data during the test in core flow with  $\theta_0 = 20^\circ$ .



**Fig. 14** Influence of the pitch angle on aerodynamic coefficients based on experimental data with different initial orientations.

vertical (lift) direction as well as the moment coefficient around the spanwise axis (pitching). These are calculated by applying Eqs. (2) and (3) with differently defined reference areas: a constant square base (Fig. 14a) and a pitch-angle-depending projected frontal area (Fig. 14b). The second one is determined by the use of Eq. (4). Additionally, trigonometric functions are fitted on these post-processed data by the method of least absolute residual. The reason for this choice of method is to weaken the effect of the measurement deviations at the dataset boundaries on the peak values of the fitting curves. For comparing, an analytic curve is added to the plots, which is determined by the modified Newtonian law as in [22].

$$S_{ref}(\theta) = l^2(|\sin(\theta)| + |\cos(\theta)|) \quad (4)$$

The presence of cube's symmetry allows to extend the results of pitch angles between  $-45^\circ$  and  $45^\circ$  on its full-rotation aerodynamic characteristics, whereby an entire period of  $90^\circ$  is considered by amalgamating the measurement data of the pitch-only configurations. As assumed by Hansche and Rinehart [7], the drag coefficient

depends on its flight attitude. These relations are demonstrated in the plots of the aerodynamic coefficients versus the pitch angle (see Fig. 14), whereby the experimental drag coefficients have its global maximum ( $C_D = 1.71$ ) at  $\theta = 0^\circ$  as well as local maxima at both sides of the graph. In comparison to the already mentioned drag coefficient ( $C_D = 1.66$ ) by Hoerner [3], the average ( $C_D = 1.64$ ) of the present study corresponds quite good with a derivation of  $-1.2\%$ . Unlike a constant value, the drag is obviously a periodic function of the pitch angle. Moreover, lift forces and pitching moments arise just for nonzero angles as well as these quantities correlate periodically with the pitch angle. Its coefficients range roughly between 0.30 and  $-0.31$  as well as between 0.04 and  $-0.06$ , respectively, having continuous curve progressions with minima and maxima. Hence, both show characteristics of negative sine functions.

By means of Fourier series, trigonometric functions with a period of  $90^\circ$  are fitted on the indirectly measured aerodynamic coefficients. This implies that the angular frequency of each Fourier term is an integer multiple of 4. However, the high-order terms are neglected due to extremely small Fourier coefficients. For the drag coefficient,

the cosine function in Eq. (5) is an approximation with an uncertainty of 0.047, reaching a maximum of 1.704 for a plane-exposed and minimum value of 1.606 for a pitch angle of  $\pm 26^\circ$ . It follows that the “flat cube” (with  $S_{\text{ref}} = l^2$ ) of Hoerner [3] is underestimated by a deviation of 2.7%. Contrary to expectations, a second local maximum with  $C_D = 1.637$  appears for an edge-exposed configuration. The detachment condition of shock waves is fulfilled here for the upper and also bottom side. Furthermore, the edge-exposed cube has the largest frontal area of all pitch-only configurations. In comparison, the modified Newtonian analysis depicts only the global maximum. However, the deviation between analytic and experimental drag coefficient is significant with a maximum absolute deviation of  $-0.368$  ( $\theta = \pm 45^\circ$ ). The reason could be that the flow in the stagnation region is subsonic and Newtonian theory is not suitable for this case.

Because of the previously shown tendencies of the measured values as well as no lift is expected for mirror-symmetric flight attitudes like  $\theta = 0^\circ$  and  $\theta = \pm 45^\circ$ , only the amplitude of the trigonometric function is considered for the regression analysis of Eq. (6), whereas phase angle and constant of the sine function are zero. Here, the lift coefficient approximation has an uncertainty of 0.043 and peak values at  $\pm 0.290$ , which is reached at the angle bisector ( $\theta = \pm 22.5^\circ$ ) of the mirror-symmetric orientations. This extreme amounts 17.0% of the maximal drag coefficient. Hence, the lift component should also be taken into account for the motion modeling of rotating cubes. The modified Newtonian theory shows a good agreement with the experimental results on lift coefficients. The maximum absolute deviation is 0.057 ( $\theta = \pm 21^\circ$ ).

Equation (7) describes the relationship of the pitch angle and its moment coefficient. The uncertainty of fitting function is 0.012. It is noticeable that the pitch angle of maximum moment appears at  $\theta = \pm 27^\circ$  and not at the angle bisector as in the  $C_L$  function. To understand its causes, the surface pressure and temperature as well as the skin friction have to be considered.

$$C_D(\theta) = 1.641 + 0.032 \cdot \cos(4\theta) + 0.031 \cdot \cos(8\theta) \quad (5)$$

$$C_L(\theta) = -0.290 \cdot \sin(4\theta) \quad (6)$$

$$C_M(\theta) = -0.040 \cdot \sin(4\theta) + 0.008 \cdot \sin(8\theta) \quad (7)$$

There are slight deviations between the experimental results and its fitted curves mainly due to marginal roll and yaw angles, as mentioned in Sec. IV.B, as well as errors becoming visible after postprocessing. Especially, the boundaries of each dataset show higher discrepancies. The reason for this is that the tracked object is located at the edges of the viewing field. Thus, less marker points are detected for an accurate geometry fitting, and the position determination of these point centers has a higher deviation. Furthermore, the mentioned causes of discrepancies are increased by less luminous intensity at the borders. In consequence, the error-prone displacement computation leads to deviations in the reconstruction of the model motion. The experimental uncertainties of the aerodynamic coefficients are determined by a simple error analysis in the present study, whereby the values base only on statistical errors of regression analysis in a  $3 - \sigma$  neighborhood. Estimated measuring uncertainties referred to the maximum value are 3% in  $C_D$ , 15% in  $C_L$ , and 28% in  $C_M$ .

It was shown previously in this study that the pitch angle has a weak effect on the drag coefficient with regard to a constant square base reference area. By referring to a pitch-angle-depending parameter, Fig. 14b takes the effective aerodynamic face area into account. Therefore, the effect of attitude on the drag is clearly visible, whereby the maximum remains the same for a plane-exposed cube, whereas the minimum with  $C_D = 1.160$  for an edge-exposed body is 29.1% below the value with constant reference area. Additionally, the aforementioned value of an edge-exposed cube is 4.5% higher than Hoerner's drag coefficient ( $C_D = 1.11$ ), whereby he referred the drag coefficient to an average projected frontal area of  $1.5l^2$  [3].

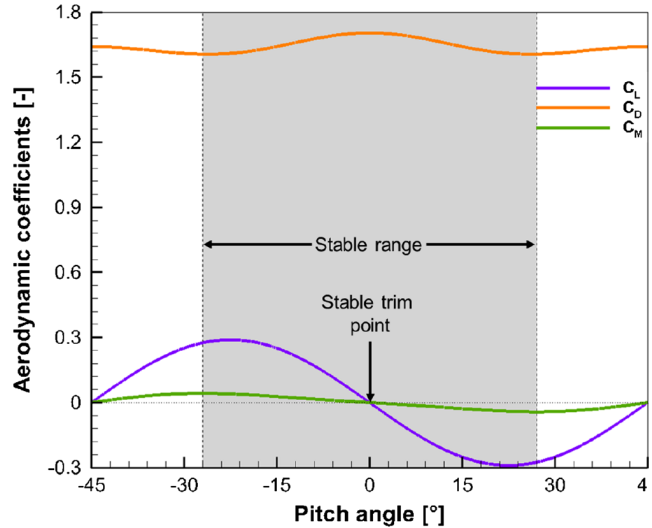


Fig. 15 Static stability depending on pitch angle.

In general, the consideration of the effective aerodynamic face area affects an absolute decline of the aerodynamic coefficients, whereas the zero and peak values occur at the same angles excepting the minimum of the drag coefficient. In relative numbers, the maxima of lift and pitching moment coefficient lie 23.5% and 25.6% below that value with constant reference area. The approximation functions of the aerodynamic coefficients referred to a projected frontal area are determined by using Eqs. (5–7) and dividing each of them by the trigonometric terms (without  $l^2$ ) of Eq. (4).

To summarize the relationships between aerodynamic coefficients and pitch angle, Fig. 15 depicts their functions from the curve fitting of a single period as well as the trim point and range of static stability. Here, the equilibrium of moments ( $C_M = 0$ ) is ensured for two orientations: plane exposed ( $\theta = 0^\circ$ ) and edge exposed ( $\theta = \pm 45^\circ$ ). Looking at the profile of pitching moment coefficients, the stable flight condition is fulfilled if an opposite moment is the response on an angle surge ( $\partial C_M / \partial \theta < 0$ ). This applies to the pitch angle interval of  $[-27^\circ, 27^\circ]$ . Both conditions are satisfied, when a cube's plane is exposed to the flow. During the present free-flight tests, the lift, drag, and pitching moment are permanently changing due to their effect on flight path angle, attitude, and velocity, which again have an impact on the aerodynamic coefficients. If a stable flight attitude is reached, the lift is zero as well as the flight attitude remains constant.

Beside this symmetrical single-degree rotation, the motion characteristics are much more complex as soon as nonzero roll and yaw angles are included. Consequently, a complete 6DoF analysis is necessary because all six aerodynamic coefficients are now a function of three orientation angles. To determine the multidimensional relationships, additional measurements have to be conducted, whereby it is useful to carry out a parametric study with two fixed angles. However, this is not possible by using the present experimental setup, because the effects of flight attitude and shear layer of the free jet lead to a three-dimensional body rotation if the vertical symmetric plane of the cube and the inflow are not parallel.

## V. Conclusions

The wind tunnel H2K at the DLR in Cologne has been successfully used to study the atmospheric reentry behavior of simple-shaped models in hypersonic flows ( $Ma_\infty = 7.0$ ) by using a free-flight technique avoiding flow interferences due to stings or balances. A stereo tracking system has been used to ensure the high-speed acquisition of 6DoF motion data consisting of positions and attitudes of the test object. For the present paper, the motion derivatives and flowfields of rotating cubic bodies have been analyzed.

The results of this study provide the evidence that the aerodynamic coefficients depend on the flight attitude, which heavily influences the flowfield around the body. Trigonometric functions with respect to the pitch angle and a period of  $90^\circ$  were fitted on the measured

values of the investigated lift, drag, and pitching moment coefficients. For a plane-exposed cube, the drag coefficient reaches its maximum with  $C_D = 1.704$ , whereby a marginal underestimation of the literature value of 2.7% was ascertained in the present study. Furthermore, it has become apparent that a not negligible lift is caused, whose peak amounts 17.0% of maximum drag coefficient. Observing the evolution of the pitching moment coefficients, a statically stable trim flight attitude was found, whereby cube's plane is exposed to the inflow. For atmospheric reentry prediction models, the findings provide data for considerable improvements, because now the aerodynamic effect of the attitude on flight path angle and velocity of a cubic body as well as a more accurate drag coefficient could be taken into account.

In the present paper, the flow characteristics of the nozzle calibration ( $Re_\infty = 8.3 \cdot 10^6 / m$ ) might be not perfectly transferable on the core flow definition of these experiments ( $Re_\infty = 2.1 \cdot 10^6 / m$ ) due to the Reynolds number effect on the shear layer thickness of the free jet. Further calibration measurements need to be done. Additionally, it should be noted that stereo tracking needs two derivations for the determination of forces and moments. Thus, a further nonintrusive technique is planned to directly measure those values with model-integrated accelerometers and gyroscopes.

These results raise a number of questions for further research. First, it remains unclear how the three orientation angles influence the 6DoF motion for complex three-degree rotations of cubes in hypersonic flowfields. Second, it would be of interest to explore certain aerodynamic effects (e.g., separation bubble and reattachment shock) downstream the leading edge in more detail to assess areas of greater loads. Because of the very small region of these effects, schlieren images with a higher magnification as well as higher resolution are suggested to determine the length of separation bubble. Furthermore, the measurement of surface pressures and temperatures is reasonable in order to assess space debris fragmentation. Finally, further tests will include also other shapes like cylinders.

### Acknowledgments

The present work has been carried out in the framework of the program *Helmholtz Research School on Security Technologies* (HRSST) and funded by the DLR (German Aerospace Center) program directorate *Defence & Security*. A fruitful collaboration with the colleges from NASA Ames Research Center's *Asteroid Threat Assessment Project* (ATAP) has benefited this work as well. The authors gratefully acknowledge the support of Michael Kosbow during the experiments and Dennis Daub for useful discussions.

### References

- [1] Charters, A. C., and Thomas, R. N., "The Aerodynamic Performance of Small Spheres from Subsonic to High Supersonic Velocities," *Journal of the Aeronautical Sciences*, Vol. 12, No. 4, 1945, pp. 468–476.  
doi:10.2514/8.11287
- [2] Hodges, A. J., "The Drag Coefficient of Very High Velocity Spheres," *Journal of the Aeronautical Sciences*, Vol. 24, No. 10, 1957, pp. 755–758.  
doi:10.2514/8.3958
- [3] Hoerner, S. F., *Fluid-Dynamic Drag: Practical Information on Aerodynamic Drag and Hydrodynamic Resistance*, 2nd ed., Hoerner Fluid Dynamics, Bakersfield, CA, 1965, pp. 16-14–16-16.
- [4] Bailey, A. B., and Hiatt, J., "Sphere Drag Coefficients for a Broad Range of Mach and Reynolds Numbers," *AIAA Journal*, Vol. 10, No. 11, 1972, pp. 1436–1440.  
doi:10.2514/3.50387
- [5] Henderson, C. B., "Drag Coefficients of Spheres in Continuum and Rarefied Flows," *AIAA Journal*, Vol. 14, No. 6, 1976, pp. 707–708.  
doi:10.2514/3.61409
- [6] Spearman, M. L., "Aerodynamics of Spheres for Mach Numbers from 0.6 to 10.5 Including Some Effects of Test Conditions," *11th Aerodynamic Decelerator Systems Technology Conference*, AIAA Paper 1991-894, 1991.  
doi:10.2514/6.1991-894
- [7] Hansche, G. E., and Rinehart, J. S., "Air Drag on Cubes at Mach Numbers 0.5 to 3.5," *Journal of the Aeronautical Sciences*, Vol. 19, No. 2, 1952, pp. 83–84.  
doi:10.2514/8.2166
- [8] Gerasimov, S. I., Erofeev, V. I., Kikeev, V. A., Gerasimova, R. V., Kanygin, I. I., and Fomkin, A. P., "Visualization of Supersonic Flow Around a Cube," *Scientific Visualization*, Vol. 7, No. 3, 2015, pp. 44–52.
- [9] Hirschel, E. H., *Basics of Aerothermodynamics*, Springer, Berlin, 2006, pp. 75–76.
- [10] Niezgodka, F.-J., "Der Hyperschallwindkanal H2K des DLR in Köln-Porz (Stand 2000)," DLR Tech. Rept. 2001-01, Köln, 2001, <https://elib.dlr.de/13874/>.
- [11] Laurence, S. J., Parziale, N. J., and Deiterding, R., "Dynamical Separation of Spherical Bodies in Supersonic Flow," *Journal of Fluid Mechanics*, Vol. 713, Dec. 2012, pp. 159–182.  
doi:10.1017/jfm.2012.453
- [12] Settles, G. S., *Schlieren and Shadowgraph Techniques*, Springer, Berlin, 2006, pp. 42–46.
- [13] McCormick, N., and Lord, J., "Digital Image Correlation," *Materials Today*, Vol. 13, No. 12, 2010, pp. 52–54.  
doi:10.1016/S1369-7021(10)70235-2
- [14] Sutton, M. A., Orteu, J. J., and Schreier, H. W., *Image Correlation for Shape, Motion and Deformation Measurements*, Springer, Boston, MA, 2009, Chap. 5.  
doi:10.1007/978-0-387-78747-3
- [15] GOM, "Digital Image Correlation and Strain Computation Basics," Tech. Rept. GOM-Gesellschaft für Optische Messtechnik mbH, 2016.
- [16] Savitzky, A., and Golay, M. J. E., "Smoothing and Differentiation of Data by Simplified Least Squares Procedures," *Analytical Chemistry*, Vol. 36, No. 8, 1964, pp. 1627–1639.  
doi:10.1021/ac60214a047
- [17] Orfanidis, S. J., *Introduction to Signal Processing*, Prentice Hall, New Brunswick, Canada, 2010, Chap. 8.3.6.
- [18] Engeln-Müllges, G., and Uhlig, F., *Numerical Algorithms with C*, Springer, Berlin, 2014, pp. 353–360.
- [19] Achner, M., "TMK Technische Notiz 04," DLR Tech. Rept. TMK-TN04, Köln, 2011.
- [20] Dyke, M. V., *An Album of Fluid Motion*, Parabolic Press, Stanford, CA, 1982, p. 166.
- [21] Halupovich, Y., Natan, B., and Rom, J., "Numerical Solution of the Turbulent Supersonic Flow over a Backward Facing Step," *Fluid Dynamics Research*, Vol. 24, No. 5, 1999, pp. 251–273.  
doi:10.1016/S0169-5983(98)00025-2
- [22] Lees, L., "Hypersonic Flow," *Journal of Spacecraft and Rockets*, Vol. 40, No. 5, 2003, pp. 700–735.  
doi:10.2514/2.6897

J. Reuther  
Associate Editor